A Tandem Reaction System for Inactivation of Marine Microorganisms by Commercial Carbon Black and Boron-Doped Carbon Nitride

Qiuchen He, Su Zhan,* and Feng Zhou*

ACCESS | Metrics & More | Article Recommendations | SI Supporting Information

ABSTRACT: The Pureballast system, based on photocatalytic technology, can purify ships' ballast water. However, the efficiency of photocatalytic sterilization still needs to be improved due to the shortcomings of the photocatalyst itself and the complex components of seawater. In this work, a tandem reaction of electrocatalytic synthesis and photocatalytic decomposition of hydrogen peroxide (H_2O_2) was constructed for the inactivation of marine microorganisms. Using seawater and air as raw materials, electrocatalytic synthesis of H_2O_2 by commercial carbon black can avoid the risk of large-scale storage and transportation of H_2O_2 on ships. In addition, boron doping can improve the photocatalytic decomposition performance of H_2O_2 by g-C_3N_4. Experimental results show that constructing the tandem reaction is effective, inactivating 99.7% of marine bacteria within 1 h. The sterilization efficiency is significantly higher than that of the single way of electrocatalysis (52.8%) or photocatalysis (56.9%). Consequently, we analyzed the reasons for boron doping to enhance the efficiency of g-C_3N_4 decomposition of H_2O_2 based on experiments and first principles. The results showed that boron doping could significantly enhance not only the transfer kinetics of photogenerated electrons but also the adsorption capacity of H_2O_2. This work can provide some reference for the photocatalytic technology study of ballast water treatment.
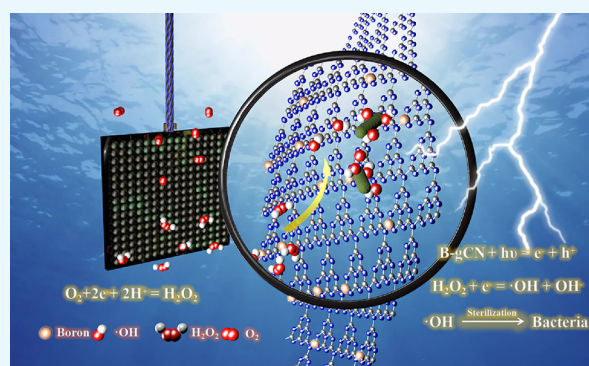
1. INTRODUCTION

The Pureballast water treatment system was the world's first ballast water treatment system to be approved by the International Maritime Organization.[1,2] It works by using photocatalytic technology to generate hydroxyl radicals, which are then used to inactivate marine microorganisms.[3,4] However, there are two significant challenges in using photocatalytic technology to treat ballast water. The first is that photocatalytic efficiency is low.[5−7] The second is that the complex components in seawater will further reduce photocatalytic efficiency.[8,9] In particular, salt can deactivate the catalyst or consume the photogenerated carrier, leading to undesirable side reactions on the catalyst surface and severely limiting the industrialization of daylight production of H_2O_2.[10,11] Both conditions limit the effectiveness of microorganisms in ballast water. The addition of hydrogen peroxide (H_2O_2) to the photocatalytic reaction system is an efficient way of improving the effectiveness of photocatalytic inactivation of ballast water. However, the large-scale H_2O_2 stored directly in the ship poses a possible safety risk to the vessel hull.[12] It is more cost-effective to manufacture H_2O_2 in ships through the two-electron oxygen reduction reaction (ORR) of electrocatalysis, using seawater and air as raw ingredients. As a result, it is critical to develop an electro-catalyst capable of producing H_2O_2 in seawater. Some reports have demonstrated that commercial carbon black is an effective catalyst for electrocatalytic H_2O_2 production,[13−16] with benefits such as high yield and low unit cost, which has some potential for future uses in ballast water management systems.

Moreover, decomposing H_2O_2 in a green way to generate hydroxyl radicals is an urgent problem that must be solved. Photocatalytic technology has become the primary choice with its environmentally friendly advantages. Since some studies have shown that unsaturated boron can effectively decompose H_2O_2 to produce hydroxyl radicals,[17,18] we attempted to synthesize boron-doped g-C_3N_4, which not only has excellent optical properties and low cost but also can be used as a boron attachment site for the carbon vacancies generated during the preparation process.[19−23]

In this paper, electrocatalytic production and photocatalytic decomposition of H_2O_2 were connected in tandem, with commercial carbon black as an electrocatalyst and boron doped g-C_3N_4 as a photocatalyst, in order to efficiently inactivate microorganisms in seawater. The experimental results indicate that carbon black in seawater may manufacture H_2O_2. The concentration of H_2O_2 may reach 5634 μM after 1 h electrocatalytic reaction at potential 0.35 V (vs RHE). g-C_3N_4 shows an H_2O_2 decomposition performance at such a concentration, greatly improving the H_2O_2 decomposition and sterilization performance of boron doped g-C_3N_4. According to dynamic studies and adsorption energy calculations, the performance enhancement is mainly attributable to an increase in the lifetime of photogenerated carriers. On the other hand, it results from the enhancement of the adsorption energy of H_2O_2. This research proposes the possibility of combining electrocatalytic production and photocatalytic decomposition of H_2O_2 in succession for the treatment of ballast water.

2. EXPERIMENTAL SECTION

2.1. Materials. The materials used in this work include melamine ($C_3H_6N_6$), cyanuric acid ($C_3H_3N_3O_3$), boric acid (H_3BO_3), epoxy resin (($C_{11}H_{12}O_3)_n$) and epoxy resin coupling agent LT560 (γ-(2,3 epoxy propoxy) propyltrimethoxysilane), methanol (CH_3OH), anhydrous ethanol (CH_3CH_2OH), 30% H_2O_2, isopropanol (C_3H_8O), EDTA-2Na ($C_{10}H_{14}N_2Na_2O_8$), 5% Nafion solution, nitric acid (HNO_3, 65%−68%), and commercial carbon black (Ketjenblack EC600; the XRD, SEM, and TEM data are shown in Figures S1−S3). These are analytically pure reagents that require no further purification. This work is made using fresh seawater from the Yellow Sea (121° 54′ E, 38° 86′ N), which has a pH of 7.9. The details of water quality parameters are shown in Table S1.

2.2. Characterization. The powder X-ray diffraction (XRD) experiment was tested by Shimadzu XRD-6100. The 2θ range was 10°−90°, the scanning step was 8°/min, the target was Cu, the working voltage was 40 kV, and the working current was 40 mA. The scanning electron microscopy (SEM) and energy dispersive spectroscopy (EDS) characterization of the sample were recorded by Thermo Scientific APREO 2C and Oxford ULTIM Max65. The working voltage was 10 kV. The sample surface was sprayed with gold. Both transmission electron microscope (TEM) and EDS were tested by FEI Talos F200S Super-X. Fourier infrared spectroscopy (FT-IR) was recorded using Thermo Fisher Nicolet IS10. UV−vis spectral analysis (UV−vis DRS) was tested using PERSEE TU-1901. The X-ray photoelectron spectroscopy (XPS) was tested with Thermo Fisher Scientific k-alpha. The vacuum degree of the analysis chamber was 5×10^{-10} Pa, the excitation source was Al K_α ray (HV = 1486.68 eV), the working voltage was 15 kV, the filament current was 10 mA, and the signal accumulation for 5−10 cycles was carried out. The passing energy was 50 eV, the step was 0.05 eV, and the charge correction was carried out with C 1s = 284.80 eV binding energy as the energy standard. The photoluminescence spectroscopy (PL) was tested by PIXEA-CU-1 (AUREA, France). The excitation wavelength was 405 nm, the repetition rate was 5 MHz, and the pulse width was 35 ps. The fluorescence signal was collected by a high-speed detector (HPM-100-50, Hamamatsu, Japan) with a 420 nm long-pass filter. The AC impedance of the sample was tested using the V-one electrochemical workstation of IVIUM (Netherlands). Potentiostatic polarization and ORR performance were tested

with CORREST CS2150H dual potentiostat. The rotating ring disk electrode (RRDE) device which was used in the ORR performance test was RRDE-1A (DEYI, Shandong). The disk electrode was made of glassy carbon (GC) with a diameter of 4 mm, and the ring electrode was made of Pt with an inner diameter of 4.3 mm and an outer diameter of 6.3 mm.

2.3. Synthesis. *2.3.1. Preparation of g-C_3N_4.* The typical high-temperature polycondensation method is used to obtain g-C_3N_4. Cyanuric acid and melamine are mixed in a mass ratio of 1:1 in 130 mL of deionized water, followed by 20 mL of isopropanol. After 30 min of ultrasonic treatment, it is completely dissolved. The solution was stirred continuously in a 70 °C water bath until the solvent completely evaporated, then it was removed, placed in a crucible, covered, and heated to 600 °C for 3 h at a rate of 10 °C/min. A light yellow powder was produced after cooling to ambient temperature.

2.3.2. Preparation of Boron Doping g-C_3N_4. 0.2 g of the above g-C_3N_4 powder was dispersed in 50 mL of deionized water. Boric acid in accordance with the mass ratio of g-C_3N_4 (the mass ratios of g-C_3N_4 are 5%, 10%, 15%, 20%, and 25%, respectively) was added. After 30 min of ultrasonic dissolution, the suspension was transferred to a polytetrafluoroethylene reactor and kept warm at 150 °C for 12 h. After removing the solvent, it was stirred and evaporated in a water bath set to 60 °C. The remaining powder was transferred to the crucible for capping and the temperature was maintained at 520 °C for 2 h at a 5 °C/min rate in air conditions by a muffle furnace. The samples were labeled as gCN, 5% B-gCN, 10% B-gCN, 15% B-gCN, 20% B-gCN, and 25% B-gCN.

2.3.3. Preparation of Photocatalyst Films. 0.1 g catalyst was uniformly disseminated in 1 mL of methanol, and 300 μL of epoxy resin and 100 μL of LT560 were added after 20 min of ultrasonic dispersion. The mixed solution was agitated for 10 min on a magnetic stirrer. The solution mentioned above was slowly added dropwise to the surface of the slides and stirred until uniformly disseminated after washing the slides with anhydrous ethanol and letting the surface dry. The slides were allowed to dry at room temperature before using and thoroughly rinsed with deionized water to remove any leftover contaminants.

2.3.4. Preparation of the EC600 Electrode. For the preparation of EC600 cathode, 10 mg of EC600 was mixed with 950 μL of isopropanol and 50 μL of Nafion solution and sonicated for 10 min to create a homogeneous mixture of carbon black, and 50 μL was applied dropwise onto 1×1 cm^2 carbon paper to obtain a catalyst loading of 0.5 mg/cm^2. Toray-060 carbon paper was utilized. Additionally, the carbon paper was pretreated with a hydrophilic treatment, which involved soaking it in HNO_3 (65−68%) at a temperature of 100 °C for 18 h and then washing it with deionized water.

For the preparation of RRDE, as mentioned above, only 5 mg of catalyst was added, and 10 μL was applied dropwise onto the GC disk electrode, with a catalyst loading of 0.2 mg/cm^2.

2.4. Electrochemical Synthesis of H_2O_2 and Sterilization Experiments. The electrochemical production of H_2O_2 was carried out in an H-shaped electrolytic cell equipped with a proton exchange membrane (Nafion 117, DuPont) in the center to isolate the working electrode and reference electrode from the counter electrode. Each side of the electrolytic cell received 50 mL of filtered fresh seawater, and the experiment started after 30 min of prepassed O_2. The reference electrode was saturated glycerol, the counter
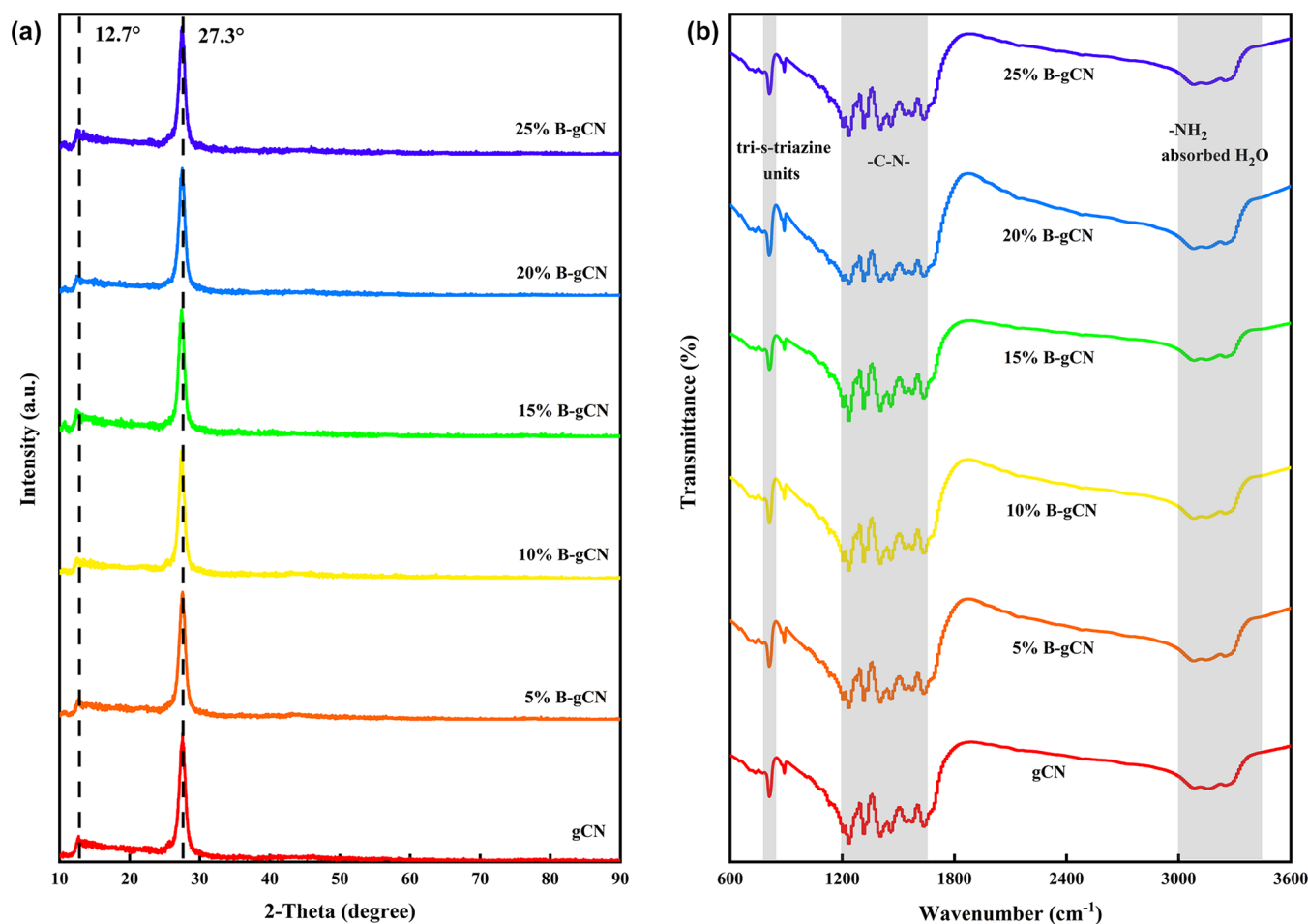
Figure 1. (a) XRD of gCN and B-gCN. (b) FT-IR of gCN and B-gCN.

electrode was a 1 × 1 cm² platinum sheet, and H_2O_2 was produced using the constant potential polarization technique. Throughout the experiment, O_2 was supplied to maintain the seawater's O_2 saturation. Before and following the experiment, 25 µL of liquid was pipet-injected onto the surface of the solid medium (see Supporting Information for medium preparation), put in a biochemical incubator, and incubated at 28 °C for 36 h. Following extraction, a colony counter (LC-JLQ-1, Lichen) was used to count the colonies. Each sample corresponded to three media, and the final resulting sterilization efficiency was the average of the three media, and the standard deviation was calculated. All essential experimental equipment was sanitized by UV before the sterilization tests. The following equation was used to get the sterilization rate:

$$\text{sterilization rate} (\%) = \frac{(S_0 - S_t)}{S_0} \times 100\% \quad (1)$$

where S_0 is the initial colony count in the seawater medium and S_t is the colony count in the medium following the sterilizing experiment.[24]

2.5. H_2O_2 Synergistic Photocatalytic Sterilization Experiment. 30 mL of fresh seawater was filtered and placed in a clear quartz container, to which a solution of 30% H_2O_2 was added and mixed well, and the produced film was applied using a 300 W Xe light source (with a 420 nm cutoff filter) with a light power of 20 mW/cm². For bacterial culture,

samples were collected before and after the light exposure, and the culture procedure was as mentioned before.

2.6. Determination of H_2O_2 Content. The H_2O_2 content was determined using cerium titration.[25−27] H_2O_2 can convert Ce^{4+} to Ce^{3+} and discolor the yellow solution, making it measurable to a UV spectrophotometer at a characteristic absorption wavelength of 318 nm. Before the quantitative analysis, a standard solution of cerium sulfate was prepared to evaluate a standard curve for measuring the H_2O_2 concentration, which is shown in Figure S4.

3. RESULTS AND DISCUSSION

3.1. Characterization. The XRD and FT-IR spectra of the samples are shown in Figure 1. Here, the XRD and FT-IR data of all samples are normalized. Figure 1a shows that all samples exhibit the typical peaks of g-C₃N₄, with the peak at 12.7° corresponding to the (100) plane of the conjugated aromatics in-plane and interlayer stacking in the triazine ring unit (JCPDS-87-1526).[28] The peak at 27.3° corresponds to the interlayer stacking reflection's (002) plane. Except for the 5% B-gCN sample, the typical peak at 12.7° of the other boron-doped samples showed a slight shift to the right, around 0.2°, indicating that boron doping may cause structural alterations in g-C₃N₄.[29] The chemical bonding vibrational modes of g-C₃N₄ are depicted in Figure 1b. The peak at 810 cm⁻¹ corresponds to the triazine ring unit's respiration mode, and the 1200−1650 cm⁻¹ wide gap corresponds to the usual stretching vibrational mode of the CN heterocycle. Additionally, the wide
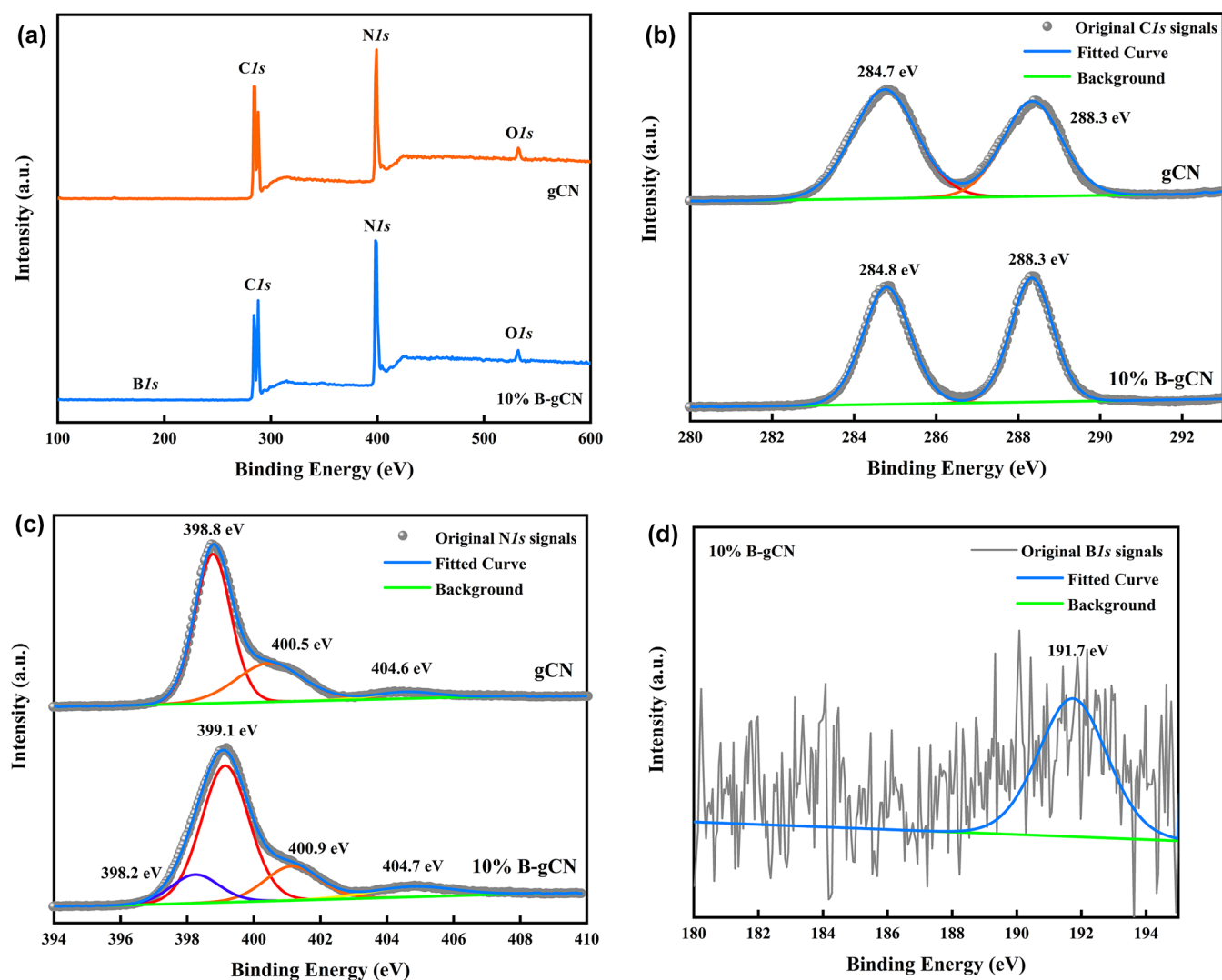
Figure 2. (a) XPS spectra of gCN and 10% B-gCN. (b) High-resolution C 1s and (c) N 1s XPS spectra of gCN and 10% B-gCN. (d) High-resolution B 1s XPS spectra of 10% B-gCN.

absorption band between 3000 and 3450 cm^{-1} corresponds to the functional group −NH$_2$ and water molecules adsorbed in the sample. In the FT-IR pattern, g-C$_3$N$_4$ does not appear to be considerably different from the boron-doped sample, which may be due to the doped boron element's low concentration.[30−32]

To confirm the presence of boron in the catalyst, XPS analysis of gCN and 10% B-gCN was performed, with the findings given in Figure 2. The total elemental spectra (Figure 2a) of both samples revealed C 1s, N 1s, and O 1s. The low boron doping induced a negligible B 1s signal in the 10% B-gCN samples, and the appropriate boron signal was reflected in the subsequent high-resolution XPS spectra. The comparison of the high-resolution C 1s spectra of the samples is depicted in Figure 2b. The binding energies of 288.3 and 284.7 eV correspond to the C=N and C−N bonds in the tri-s-triazine structure, respectively.[33,34] The high-resolution N 1s spectrum of the sample is shown in Figure 2c, where the peaks at 398.8, 400.5, and 404.6 eV correspond to the N−C bond, N=C bond, and π-excitations in the heterocycles in gCN, respectively, whereas the peaks representing the N−C bond (399.1 eV) and N=C bond (400.9 eV) in 10% B-gCN are shifted toward the high binding energy, indicating that boron

has effected the tri-s-triazine structure.[35,36] This result is also in response to the previous XRD data. Furthermore, B−N bonds were identified in the N 1s and B 1s (Figure 2d) high-resolution spectra of 10% B-gCN by signals of 398.2 and 191.7 eV, indicating that boron-doped gCN was produced in this work and that the boron element partially replaced the carbon in gCN.[22,32,37] To further describe the boron distribution, we performed SEM and TEM experiments, the results of which are presented in Figure 3. The morphology of gCN did not change considerably following boron doping (Figure 3a,b). However, the elemental mapping of 10% B-gCN clearly shows the distribution of boron, nitrogen, and carbon components, consistent with the TEM observations (Figure 3c,d), demonstrating the successful boron doping into gCN once again.

A comparison of the UV−vis DRS plots of gCN and B-gCN is shown in Figure 4a, which indicates that boron doping does not affect the light absorption characteristics of gCN.[38] According to the Kubelka−Munk method, the DRS plot may be converted into Tauc plots (Figure S5), and the prohibited bandwidth is between 2.78 and 2.83 eV. The Mott−Schottky method was used to investigate the flat-band (FB) potentials of gCN and 10% B-gCN samples to calculate their valence band
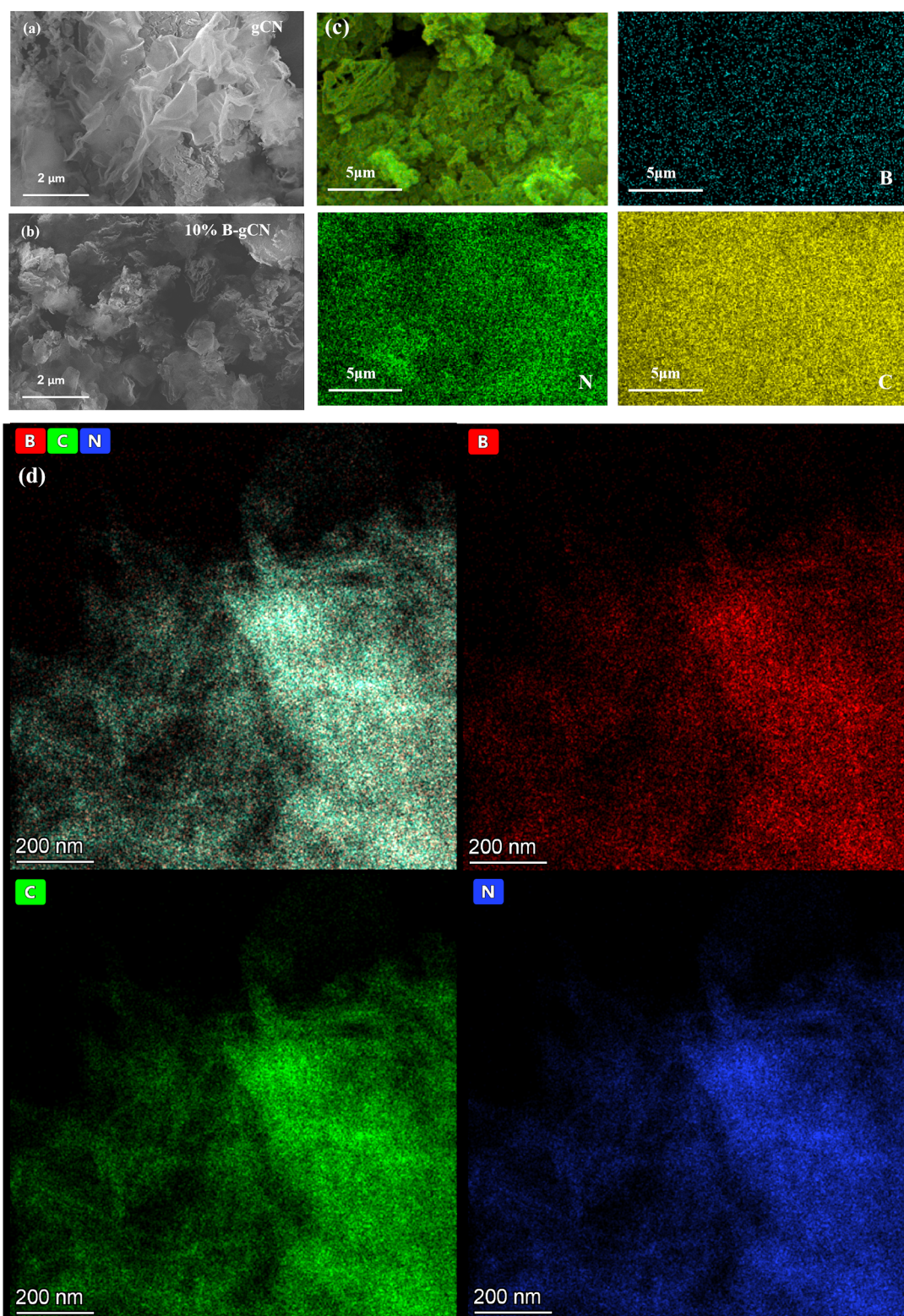
Figure 3. SEM images of (a) gCN and (b) 10% B-gCN. (c) Elemental distribution in the mapping plot for 10% B-gCN. (d) TEM elemental mapping images of 10% B-gCN.

(VB) and conductive band (CB).[39] The result shows that the FB values of these two samples are −1.01 and −0.90 V (vs RHE), respectively (Figure 4b). When coupled with the result of Tauc plots, the VB and CB for gCN are −1.01 and 1.77 V (vs RHE) and for 10% B-gCN are −0.90 and 1.88 V (vs RHE), respectively.

3.2. Catalytic Performance. In this section, we used EC600 as an electrocatalyst in a photoelectric tandem system to generate H_2O_2. A tandem of tests was done to understand the performance of H_2O_2 generation better. All the potential units were converted into reversible hydrogen electrodes (RHE) in the following figures. The findings of the cyclic
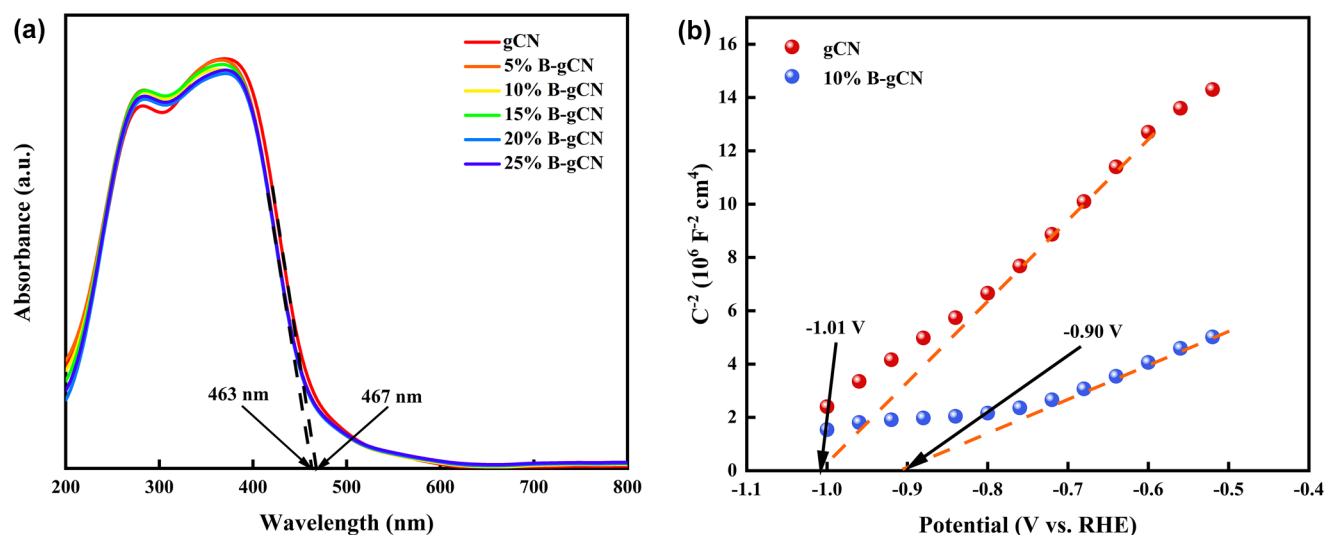
Figure 4. (a) UV−vis DRS plot of gCN and B-gCN. (b) Mott−Schottky plots of gCN and 10% B-gCN.
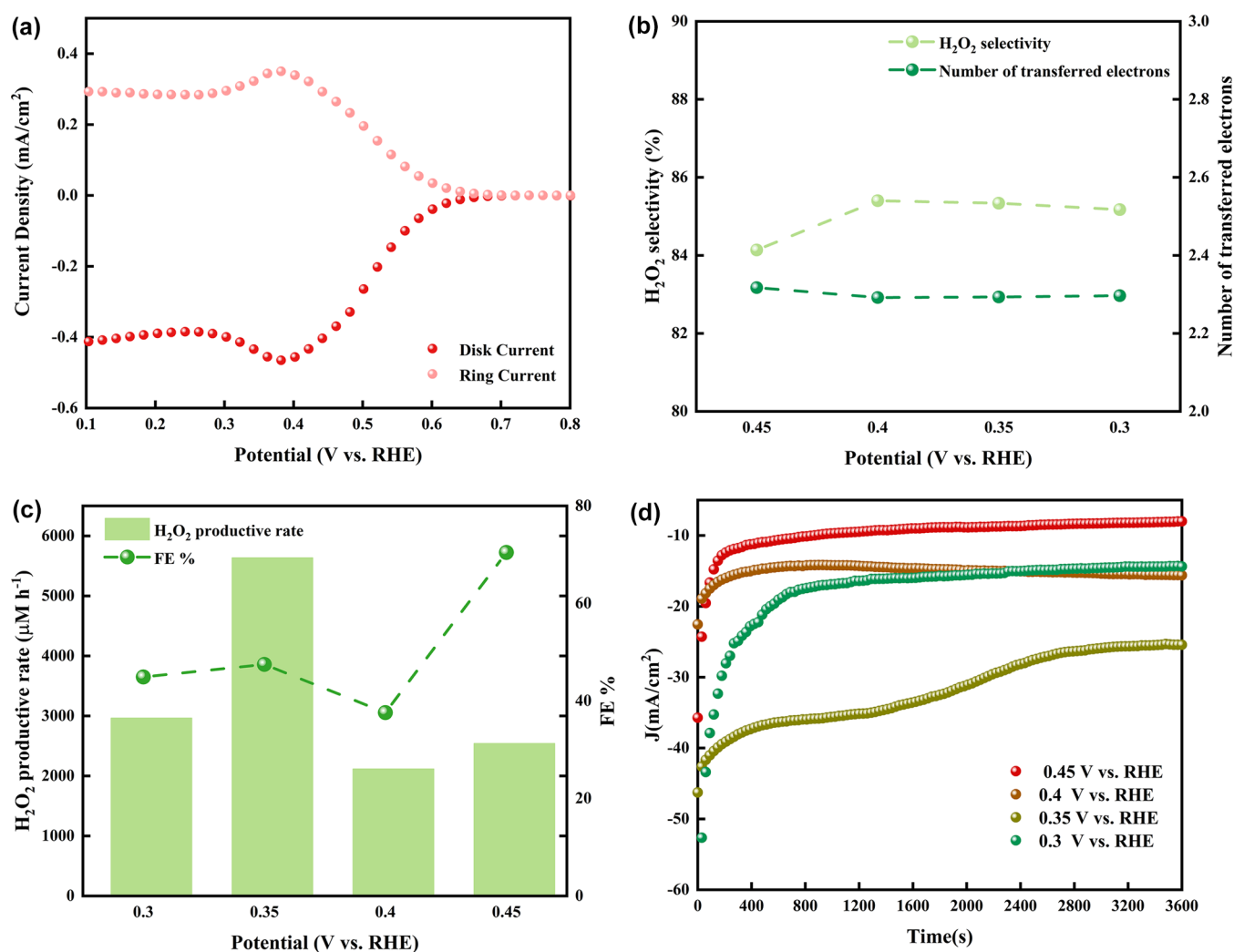
Figure 5. Electrochemical ORR performance of EC600 in O_2 saturated seawater pH = 7.9. (a) LSV at 1600 rpm (red line) and the simultaneous H_2O_2 detection current density (after N correction) at the ring electrode (pink line). (b) Calculated electron transfer number and H_2O_2 selectivity. (c) H_2O_2 productive rate and Faradaic efficiencies for the ORR at different potentials. (d) Time-dependent current density curves of EC600 at different potentials.
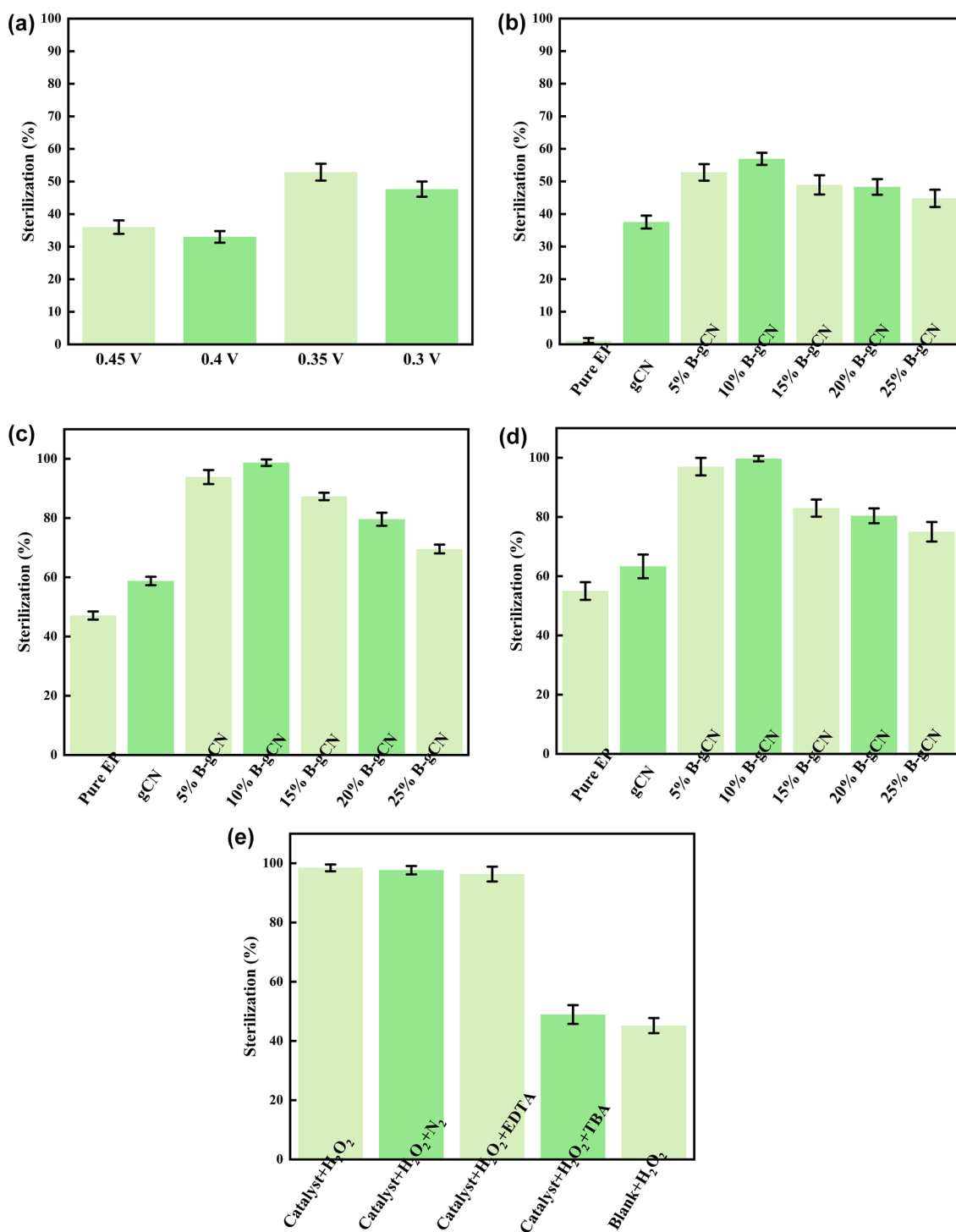
Figure 6. (a) Electrocatalytic sterilization at different potentials. (b) Photocatalytic sterilization of pure EP, gCN, and B-gCN. (c) Photocatalytic decomposition of H_2O_2 sterilization of pure EP, gCN, and B-gCN. (d) Tandem electrocatalytic and photocatalytic sterilization of pure EP, gCN, and B-gCN. (e) Free radical capture test.

voltammetric (CV) curve tests, which were conducted under N_2 and O_2 saturation circumstances, are described in Figure S6. The redox peak of the sample was not seen at the N_2 saturation condition, suggesting that the sample does not react in seawater.

In comparison, under O_2 saturated conditions, a significant oxygen reduction peak was observed at 0.41 V(vs RHE) for the negative sweep curve. No significant current change was observed for the positive sweep curve, indicating that the

sample can reduce oxygen without being oxidized by it.[40,41] Earlier studies demonstrated the limits of the Koutechy– Levich method in estimating the oxygen reduction selectivity and transfer electron number,[42] thus the current work applied a RRDE to assess the oxygen reduction performance of the catalyst, with a catalyst loading of 0.1 mg cm^{-2} at 1600 rpm and fresh seawater as the electrolyte (pH = 7.9). The collection coefficient (N) of the Pt ring was tested using the redox reaction $[Fe(CN_6)_4]^-/[Fe(CN_6)_3]^-$ to make the RRDE

experiment results more accurate. It was calculated by using the equation below:[43]

$$N = \left| \frac{I_{r,[\text{Fe(II)(CN)}]^{4-}}}{-I_{d,[\text{Fe(III)(CN)}]^{3-}}} \right| \tag{2}$$

where I_r is the current of the ring, and the I_d is the current of the disk. The result is shown in Figure S7. Figure 5a shows the linear scanning voltammetric curve measured using RRDE, with the ring current calibrated by the collection coefficient (0.30) in the upper half and the disk current in the lower half. The limiting current plateau of the catalyst occurs at 0.4 V. Therefore, we calculated the number of electrons transferred and the H_2O_2 selectivity of the catalyst at potentials of 0.3, 0.35, 0.4, and 0.45 V(vs RHE), respectively, according to the following equations for the number of electrons transferred[44] and the H_2O_2 selectivity:[45]

$$n = \frac{4I_d}{I_d + (I_r/N)} \tag{3}$$

$$H_2O_2\% = \frac{2I_r/N}{I_d + I_r/N} \times 100\% \tag{4}$$

where I_r is the current of the ring, I_d is the current of the disk, and N is the collection coefficient of the Pt ring ($N = 0.30$). The results are summarized in Figure 5b and Table S2.

To determine the quantity of H_2O_2 produced in a simple device, we put EC600 onto carbon paper (with a loading of 0.5 mg cm^{-2}) and tested it in an H-type electrolytic cell filled with fresh seawater. Figure 5c illustrates the associated H_2O_2 yields and Faraday efficiencies at various potentials. The corresponding time−current curve is shown in Figure 5d. At 0.45 V (vs RHE), the EC600 electrode has a maximum Faraday efficiency of 70.5%, equivalent to an H_2O_2 production rate of 2540 μM h^{-1}. The highest yield of 5634 μM h^{-1} was obtained at 0.35 V (vs RHE) potential, but the Faraday efficiency was significantly lower at 47.5%. It is noteworthy that some white flocculent precipitates were produced during the reaction at each potential. Moreover, a large amount of white flocculent precipitated on the electrode surface during the reaction at a potential of 0.4 V (vs RHE). Eventually, it covered the electrode surface with the increase of reaction time. We collected and analyzed the white flocculent precipitation on the electrode surface and electrolytic cells, including SEM images, EDS (Figure S8), HRTEM images, corresponding EDS elements (Figure S9), and ICP-OES (Table S3). The results showed that the main elements of this white flocculent precipitation were Mg and O, with small amounts of Na, K, Ca, Cl, and S elements. This explains why the Faraday efficiency drops noticeably below or equivalent to 0.4 V (vs RHE).

In the 0.3−0.45 V (vs RHE) potential interval, the corresponding H_2O_2 concentrations in the H-type electrolytic cell were 2540, 2116, 5634, and 2964 μM h^{-1}, respectively. To test the inactivation performance of H_2O_2 concentration on marine bacteria, 25 μL of seawater from the H-type electrolytic cell was taken in the solid medium for incubation, and the sterilization efficiency is summarized in Figure 6a. The result reveals that the higher the concentration of H_2O_2, the higher the sterilization performance. When the concentration is 5634 μM, the sterilizing efficiency is 52.8% (see Figure S10), insufficient for H_2O_2 decomposition alone. In order to test the stability of the EC600 electrode for H_2O_2 production, an

additional 10 cycles of stability testing was performed on the same EC600 electrode. Before the test, the electrode surface was rinsed with deionized water to remove white flocculent precipitates. Each test was conducted for 1 h, and fresh seawater was replaced. As shown in Figure S11, the EC600 electrode showed a 49% decrease in H_2O_2 production rate after the first test and a relatively stable H_2O_2 production rate of 2627 μM h^{-1} (average) in the subsequent tests. Furthermore, as the H_2O_2 production rate decreased, the Faraday efficiency improved from 46% in the first test to 61% (average). This may be caused by the decrease of H_2O_2 production rate on the electrode surface, resulting in less white flocculent precipitation.

To further improve the sterilizing efficiency, we utilized the photocatalyst to enhance the decomposition of H_2O_2 to generate hydroxyl radicals. Furthermore, we built a tandem reaction for electrocatalytic synthesis and photocatalytic decomposition of H_2O_2. First, we tested the sterilization performance of the photocatalytic system. The photocatalyst coating by combining the catalyst with epoxy resin painting was prepared. We then tested the sterilization performance of pure epoxy resin coating (EP) and photocatalyst coating under visible light-only conditions ($\lambda > 420$ nm). The results indicated that pure epoxy resin coating (EP) had almost no sterilization effect, excluding the possibility of pure epoxy resin coating interference. All photocatalytic coatings exhibited quantified sterilization performance, and B-gCN outperformed g-CN, with the best sterilization effect of 56.9% for 10% B-gCN, which is summarized in Figure 6b. The corresponding photos of the media are shown in Figure S12. We then added H_2O_2 to the photocatalytic system. The H_2O_2 concentration here was the maximum for electrocatalytic H_2O_2 generation in the above experiment. After 1 h of photocatalytic sterilization, the sterilization performance of all samples was significantly improved, with the sterilization efficiency of 10% B-gCN reaching 98.7%, which was significantly better than the sterilization efficiency of gCN (Figure 6c and Figure S13). Photocatalytic decomposition of H_2O_2 sterilization efficiency was significantly higher than the sterilization efficiency of single way. Finally, we verified the performance of the tandem system. After electrocatalytic synthesis of H_2O_2 at 0.35 V vs RHE potential, the treated seawater was added directly to a reaction vessel containing a photocatalytic film. The results are shown in Figure 6d and Figure S14. The sterilization efficiency of the tandem system was similar to that of H_2O_2 photocatalytic decomposition (99.7%). The result indicates the feasibility of constructing a tandem system of electrocatalytic synthesis and photocatalytic decomposition of H_2O_2 for the inactivation of marine microorganisms.

In order to analyze the sterilization mechanism, we performed a free radical capture experiment. The findings of free radical capture tests in seawater containing 5600 μM H_2O_2 are depicted in Figure 6e and Figure S15. When no photocatalyst was used, the sterilizing effectiveness was 45.2%. This result was comparable to the electrocatalytic sterilization efficiency only. EDTA and TBA were used as radical trapping agents for superoxide and hydroxyl radicals, respectively. With the addition of EDTA, the photocatalytic sterilization efficiency was maintained at 96.3%. Whereas with the addition of TBA, the photocatalytic sterilization efficiency fell dramatically to 48.9%. It implies that the primary mechanism by which marine bacteria are inactivated is the generation of hydroxyl radicals in the system. When combined
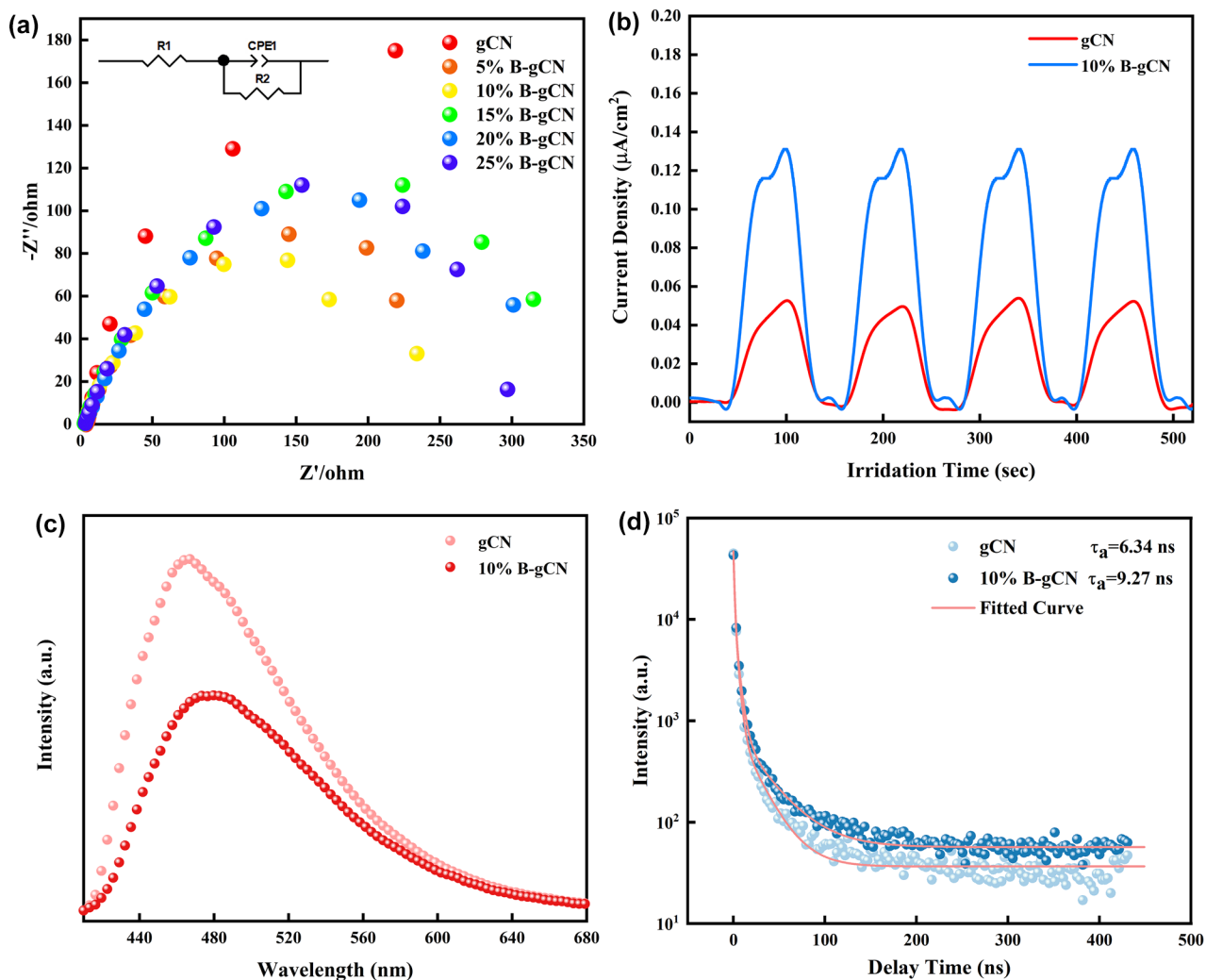
Figure 7. (a) EIS Nyquist plots of gCN and B-gCN. (b) Transient photocurrent response spectra of gCN and 10% B-gCN. (c) PL spectra of gCN and 10% B-gCN. (d) Time-resolved fluorescence spectroscopy of gCN and 10% B-gCN.

with the analysis of DRS and Mott−Schottky data, it was determined that the VB of 10% B-gCN was insufficient to generate hydroxyl radicals.[46−48] Thus, the hydroxyl radicals in the system originated from the decomposition of H_2O_2 by photocatalyst. Both electrocatalytic synthesis and photocatalytic decomposition of H_2O_2 played a significant role in the entire sterilization system, contributing to the system's high efficacy.

To analyze the effect of boron doping on the electron transfer kinetics of g-C_3N_4, we performed EIS, transient photocurrent, photoluminescence and time-resolved fluorescence spectroscopy tests. As shown in Figure 7a-b, B-gCN resulted in a substantial decrease in the EIS arc radius and an increased in the transient photocurrent density. The equivalent circuit diagram was obtained by fitting EIS data. In the equivalent circuit diagram, R1 represents solution resistance R_s, and R2 represents charge-transfer resistance R_{ct}. 10% B-gCN shows the lowest R_{ct}, and this indicated that boron doping could improve the efficiency of electron transfer. The corresponding data are shown in Table S4. The photoluminescence intensity was substantially decreased after boron doping, and third-order exponential fitting was used to evaluate the time-resolved fluorescence lifetimes of the samples (Figure 7c,d). gCN and 10% B-gCN had fluorescence durations of 6.34

and 9.27 ns, respectively. The details fitting parameters are shown in Table S5. Additionally, the EIS and photocurrent results show that the presence of H_2O_2 may enhance the photogenerated carrier separation efficiency of the catalysts. Figure S16 and Table S4 illustrate the EIS plots and R_{ct} of several catalysts in seawater with and without H_2O_2. When H_2O_2 is present in seawater, the EIS arc radii and R_{ct} all decrease substantially, indicating that H_2O_2 may serve as an acceptor for photogenerated electrons, thus increasing the surface reaction efficiency of the catalysts. Photocurrent curves also confirm this conclusion, shown in Figure S17.

Numerous previous studies have established that g-C_3N_4 can synthesize H_2O_2 via two-step single electron transfer or one-step two electrons transfer in a photocatalytic system,[49−52] but our results appear to contradict previous findings. One possible explanation is that when the H_2O_2 concentration in the solution exceeds a specific value, O_2 and H_2O_2 will compete for adsorption on the catalyst surface. When combined with DRS and Mott−Schottky data, it is demonstrated that boron doping can increase the efficiency of photogenerated carrier separation without altering the band structure of g-C_3N_4. B-gCN has a higher H_2O_2 decomposition and sterilization ability in a certain concentration of H_2O_2.
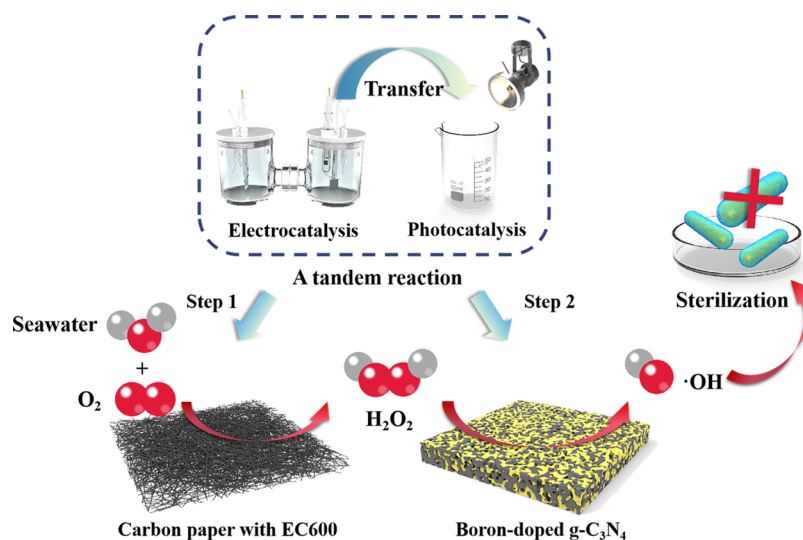
Figure 8. Schematic diagram of electrocatalytic synthesis of H_2O_2 and photocatalytic decomposition of H_2O_2 in a tandem reaction.

3.3. Calculation. To seek a reasonable explanation for our conjecture, we finally used the first-principles calculations to compare the adsorption energies of O_2 and H_2O_2 on the catalyst surface. The calculations were carried out in Materials Studio using the CASTEP module with a cutoff energy of 630 eV and a k-point of $2 \times 2 \times 3$.[53,54] Figure S18 illustrates the built adsorption model, and the total energy of cells was summarized in Table S6. The equation of absorption energy is the following:

$$E_{ab.} = E_{total} - E_{O_2/H_2O_2} - E_{cat.} \tag{5}$$

where $E_{ab.}$ is the adsorption energy, E_{total} is the total cell energy after adsorption of the substance, E_{O_2/H_2O_2} is the cell energy of O_2 or H_2O_2, and $E_{cat.}$ is the cell energy of the catalyst. The calculated results revealed that the adsorption energies of H_2O_2 and O_2 on the gCN surface are -0.81 eV and -0.97 eV, respectively, with a difference of 0.16 eV between them. When the H_2O_2 concentration in the solution system is low, the gCN surface will preferentially adsorb O_2 to produce H_2O_2. After boron doping, the adsorption energies of H_2O_2 and O_2 on the B-gCN surface were -0.57 eV and -0.61 eV, respectively, with a significant difference of just 0.04 eV, indicating that boron doping was more favorable for H_2O_2 adsorption on the catalyst surface. Furthermore, when the concentration of H_2O_2 in the solution system reaches a certain value, H_2O_2 and O_2 compete for adsorption on the surface of the B-gCN catalyst. As the concentration of H_2O_2 increases, the catalyst eventually exhibits significant H_2O_2 decomposition, which is consistent with the sterilization results. The surface's differential charge density diagram (Figure S19) can see the electron transfer from the boron and nitrogen atoms to the H_2O_2, which indicates that the boron and nitrogen atoms can act as the decomposition center of H_2O_2.

Based on experimental results and theoretical calculation, the schematic diagram of electrocatalytic synthesis and photocatalytic decomposition of H_2O_2 tandem reaction is shown in Figure 8. As a first step, the electrocatalytic reaction can use O_2 and seawater as raw materials to synthesize H_2O_2 by the commercial electrocatalyst EC600 at a proper potential. The second step, photocatalysis can effectively decompose H_2O_2 and convert it into hydroxyl radicals. During the photocatalytic reaction, H_2O_2 acts not only as a source of

hydroxyl radicals but also as an electron acceptor for the photocatalyst, which effectively improves the separation efficiency of photogenerated carriers. Effective inactivation of marine bacteria can be achieved by a two-step reaction in tandem. At the same time, sterilization efficiency is much lower when using the only electrocatalytic synthesis of H_2O_2 for sterilization or only photocatalytic reaction for sterilization.

4. CONCLUSIONS

This work developed a tandem reaction for the electrocatalytic production and photocatalytic decomposition of H_2O_2 using commercial carbon black (EC600) as an electrocatalyst and B-gCN as a photocatalyst and applied it to the treatment of marine microorganisms. In seawater, EC600 demonstrated a two-electron ORR performance. After a 1 h of electrocatalytic reaction, the H_2O_2 concentration in seawater could reach 5634 μM, inactivating 52.8% of marine bacteria in the reaction system. While B-gCN can decompose H_2O_2 into hydroxyl radicals in the photocatalytic system, 99.7% of marine bacteria can be inactivated within 1 h in the tandem reaction system. It suggests that creating a tandem reaction is a viable method. Moreover, based on experimental data and first-principles calculations, it can be inferred that following boron doping, the transfer kinetics of g-C_3N_4 photogenerated electrons can be considerably improved. In contrast, the adsorption capacity of the catalyst for H_2O_2 can be improved. When the concentration of H_2O_2 in the solution reaches a certain value, the B-doped g-C_3N_4 demonstrates efficient photocatalytic decomposition of H_2O_2.

■ ASSOCIATED CONTENT

Ⓢ **Supporting Information**

The Supporting Information is available free of charge at https://pubs.acs.org/doi/10.1021/acsomega.2c00679.

> Detailed information on culture media production methods and some characterization equipment; characterization data of EC600; hydrogen peroxide standard curve; DRS, photocurrent, and EIS data of photocatalysts; characterization of white flocculent precipitates; details of the first-principles calculation; water quality parameters of fresh seawater; and culture media photos of the sterilization experiment (PDF)

■ AUTHOR INFORMATION

Corresponding Authors

Su Zhan − *Key Laboratory of Ship-Machinery Maintenance and Manufacture, Ministry of Transport, Dalian Maritime University, Dalian 116026, PR China*; Email: zhans@dlmu.edu.cn

Feng Zhou − *Key Laboratory of Ship-Machinery Maintenance and Manufacture, Ministry of Transport, Dalian Maritime University, Dalian 116026, PR China*; ⊙ orcid.org/0000-0002-1715-2380; Email: zhoufeng@dlmu.edu.cn

Author

Qiuchen He − *Key Laboratory of Ship-Machinery Maintenance and Manufacture, Ministry of Transport, Dalian Maritime University, Dalian 116026, PR China*

Complete contact information is available at:
https://pubs.acs.org/10.1021/acsomega.2c00679

Notes

The authors declare no competing financial interest.

■ ACKNOWLEDGMENTS

■ REFERENCES

(1) Warg, P. Retrofitting PureBallast Water Treatment Systems onboard Two Car Carriers. *Journal of the Japan Institute of Marine Engineering* **2011**, *46* (4), 585−589.

(2) Ballast treatment can destroy harmful micro-organisms. *Filtr. Sep.* **2007**, *44*, 10.

(3) Zhan, S.; Zhou, F.; Huang, N.; He, Q.; Zhu, Y. Deactivating harmful marine microorganisms through photoelectrocatalysis by GO/ZnWO$_4$ electrodes. *Chem. Eng. J.* **2017**, *330*, 635−643.

(4) Bai, M.; Zhang, Z.; Zhang, N.; Tian, Y.; Chen, C.; Meng, X. Treatment of 250 t/h ballast water in oceanic ships using ·OH radicals based on strong electric-field discharge. *Plasma Chem. Plasma Process* **2012**, *32* (4), 693−702.

(5) Ebihara, M.; Ikeda, T.; Okunaka, S.; Tokudome, H.; Domen, K.; Katayama, K. Charge carrier mapping for Z-scheme photocatalytic water-splitting sheet via categorization of microscopic time-resolved image sequences. *Nat. Commun.* **2021**, *12* (1), 3716.

(6) Li, J.; Li, Z.; Liu, X.; Li, C.; Zheng, Y.; Yeung, K. W. K.; Cui, Z.; Liang, Y.; Zhu, S.; Hu, W.; et al. Interfacial engineering of Bi$_2$S$_3$/Ti$_3$C$_2$T$_x$ MXene based on work function for rapid photo-excited bacteria-killing. *Nat. Commun.* **2021**, *12* (1), 1224.

(7) Liang, Z.; Shen, R.; Ng, Y. H.; Zhang, P.; Xiang, Q.; Li, X. A review on 2D MoS$_2$ cocatalysts in photocatalytic H$_2$ production. *J. Mater. Sci. Technol.* **2020**, *56*, 89−121.

(8) Ayyub, M. M.; Chhetri, M.; Gupta, U.; Roy, A.; Rao, C. Photochemical and photoelectrochemical hydrogen generation by splitting seawater. *Chem. Eur. J.* **2018**, *24* (69), 18455−18462.

(9) Zhu, C.; Liu, C.; Fu, Y.; Gao, J.; Huang, H.; Liu, Y.; Kang, Z. Construction of CDs/CdS photocatalysts for stable and efficient hydrogen production in water and seawater. *Appl. Catal., B* **2019**, *242*, 178−185.

(10) Wu, Q.; Cao, J.; Wang, X.; Liu, Y.; Zhao, Y.; Wang, H.; Liu, Y.; Huang, H.; Liao, F.; Shao, M.; Kang, Z. A metal-free photocatalyst for highly efficient hydrogen peroxide photoproduction in real seawater. *Nat. Commun.* **2021**, *12* (1), 483.

(11) Tsoi, C. C.; Huang, X.; Leung, P. H. M.; Wang, N.; Yu, W.; Jia, Y.; Li, Z.; Zhang, X. Photocatalytic ozonation for sea water decontamination. *J. Water Process.* **2020**, *37*, 101501.

(12) Moreno-Andrés, J.; Romero-Martínez, L.; Acevedo-Merino, A.; Nebot, E. Determining disinfection efficiency on E. faecalis in saltwater by photolysis of H$_2$O$_2$: Implications for ballast water treatment. *Chem. Eng. J.* **2016**, *283*, 1339−1348.

(13) Chen, S.; Wei, K.; Wang, Y.; Wang, J.; Huang, H.; Huang, X.; Logan, B. E.; Zhang, X. Enhanced recalcitrant pollutant degradation using hydroxyl radicals generated using ozone and bioelectricity-driven cathodic hydrogen peroxide production: Bio-E-Peroxone process. *Sci. Total Environ.* **2021**, *776*, 144819.

(14) Li, N.; An, J.; Zhou, L.; Li, T.; Li, J.; Feng, C.; Wang, X. A novel carbon black graphite hybrid air-cathode for efficient hydrogen peroxide production in bioelectrochemical systems. *J. Power Sources* **2016**, *306*, 495−502.

(15) Chen, J.; Li, N.; Zhao, L. Three-dimensional electrode microbial fuel cell for hydrogen peroxide synthesis coupled to wastewater treatment. *J. Power Sources* **2014**, *254*, 316−322.

(16) Chen, Z.; Dong, H.; Yu, H.; Yu, H. In-situ electrochemical flue gas desulfurization via carbon black-based gas diffusion electrodes: Performance, kinetics and mechanism. *Chem. Eng. J.* **2017**, *307*, 553−561.

(17) Li, H.; Li, Y.; Sun, L.; Xun, S.; Jiang, W.; Zhang, M.; Zhu, W.; Li, H. H$_2$O$_2$ decomposition mechanism and its oxidative desulfurization activity on hexagonal boron nitride monolayer: A density functional theory study. *J. Mol. Graph. Model.* **2018**, *84*, 166−173.

(18) Quintanilla, A.; Vega, G.; Carbajo, J.; Casas, J. A.; Lei, Y.; Fujisawa, K.; Liu, H.; Cruz-Silva, R.; Terrones, M.; Miranzo, P.; et al. Understanding the active sites of boron nitride for CWPO: An experimental and computational approach. *Chem. Eng. J.* **2021**, *406*, 126846.

(19) Liu, Z.; Liu, J.; Mateti, S.; Zhang, C.; Zhang, Y.; Chen, L.; Wang, J.; Wang, H.; Doeven, E. H.; Francis, P. S.; et al. Boron radicals identified as the source of the unexpected catalysis by boron nitride nanosheets. *ACS Nano* **2019**, *13* (2), 1394−1402.

(20) Jin, Z.; Zhang, L. Performance of Ni-Cu bimetallic co-catalyst g-C$_3$N$_4$ nanosheets for improving hydrogen evolution. *J. Mater. Sci. Technol.* **2020**, *49*, 144−156.

(21) Wang, X.; Blechert, S.; Antonietti, M. Polymeric graphitic carbon nitride for heterogeneous photocatalysis. *ACS Catal.* **2012**, *2* (8), 1596−1606.

(22) Bao, H.; Wang, L.; Li, G.; Zhou, L.; Xu, Y.; Liu, Z.; Wu, M. Carrier engineering of carbon nitride boosts visible-light photocatalytic hydrogen evolution. *Carbon* **2021**, *179*, 80−88.

(23) Sagara, N.; Kamimura, S.; Tsubota, T.; Ohno, T. Photoelectrochemical CO$_2$ reduction by a p-type boron-doped g-C$_3$N$_4$ electrode under visible light. *Appl. Catal., B* **2016**, *192*, 193−198.

(24) Wang, F.; Song, Y.; He, Q.; Zhang, C.; Lai, J.; Zhan, S.; Zhou, F. Performance tuning and optimization of 2D-2D-like g-C$_3$N$_4$ modified Bi$_2$O$_2$CO$_3$ n-n homotypic heterojunction as an inactivating photocatalytic material. *J. Environ. Chem. Eng.* **2021**, *9*, 106176.

(25) Chen, S.; Luo, T.; Chen, K.; Lin, Y.; Fu, J.; Liu, K.; Cai, C.; Wang, Q.; Li, H.; Li, X.; et al. Chemical Identification of Catalytically Active Sites on Oxygen-doped Carbon Nanosheet to Decipher the High Activity for Electro-synthesis Hydrogen Peroxide. *Angew. Chem., Int. Ed.* **2021**, *60*, 16607−16614.

(26) Sun, F.; Yang, C.; Qu, Z.; Zhou, W.; Ding, Y.; Gao, J.; Zhao, G.; Xing, D.; Lu, Y. Inexpensive activated coke electrocatalyst for high-efficiency hydrogen peroxide production: Coupling effects of amorphous carbon cluster and oxygen dopant. *Appl. Catal., B* **2021**, *286*, 119860.

(27) Zhang, C.; Zhou, F.; Zhan, S.; Song, Y.; Wang, F.; Lai, J. The enhanced photocatalytic inactivation of marine microorganisms over ZnO supported Ag quantum dots by the synthesis of H$_2$O$_2$. *Environ. Res.* **2021**, *197*, 111129.

(28) Zhang, S.; Gao, L.; Fan, D.; Lv, X.; Li, Y.; Yan, Z. Synthesis of boron-doped g-C$_3$N$_4$ with enhanced electro-catalytic activity and stability. *Chem. Phys. Lett.* **2017**, *672*, 26−30.

(29) Thorat, N.; Yadav, A.; Yadav, M.; Gupta, S.; Varma, R.; Pillai, S.; Fernandes, R.; Patel, M.; Patel, N. Ag loaded B-doped-g C$_3$N$_4$

nanosheet with efficient properties for photocatalysis. *J. Environ. Manage.* **2019**, *247*, 57−66.

(30) Yang, Y.; Zhang, C.; Huang, D.; Zeng, G.; Huang, J.; Lai, C.; Zhou, C.; Wang, W.; Guo, H.; Xue, W.; et al. Boron nitride quantum dots decorated ultrathin porous g-C_3N_4: intensified exciton dissociation and charge transfer for promoting visible-light-driven molecular oxygen activation. *Appl. Catal., B* **2019**, *245*, 87−99.

(31) Zhang, M.; Yang, L.; Wang, Y.; Li, L.; Chen, S. High yield synthesis of homogeneous boron doping C_3N_4 nanocrystals with enhanced photocatalytic property. *Appl. Surf. Sci.* **2019**, *489*, 631−638.

(32) Wei, J.; Shen, W.; Zhao, J.; Zhang, C.; Zhou, Y.; Liu, H. Boron doped g-C_3N_4 as an effective metal-free solid base catalyst in Knoevenagel condensation. *Catal. Today* **2018**, *316*, 199−205.

(33) Kong, W.; Zhang, X.; Chang, B.; Zhou, Y.; Zhang, S.; He, G.; Yang, B.; Li, J. Fabrication of B doped g-C_3N_4/TiO_2 heterojunction for efficient photoelectrochemical water oxidation. *Electrochim. Acta* **2018**, *282*, 767−774.

(34) Zeng, W.; Bian, Y.; Cao, S.; Zhu, A.; Qiao, L.; Ma, Y.; Tan, P.; Ma, Q.; Dong, R.; Pan, J. Construction of two dimensional $Sr_2Ta_2O_7$/S-doped g-C_3N_4 nanocomposites with Pt cocatalyst for enhanced visible light photocatalytic performance. *Appl. Surf. Sci.* **2019**, *478*, 334−340.

(35) Liu, M.; Jiao, Y.; Qin, J.; Li, Z.; Wang, J. Boron doped C_3N_4 nanodots/nonmetal element (S, P, F, Br) doped C_3N_4 nanosheets heterojunction with synergistic effect to boost the photocatalytic hydrogen production performance. *Appl. Surf. Sci.* **2021**, *541*, 148558.

(36) Huang, D.; Li, Z.; Zeng, G.; Zhou, C.; Xue, W.; Gong, X.; Yan, X.; Chen, S.; Wang, W.; Cheng, M. Megamerger in photocatalytic field: 2D g-C_3N_4 nanosheets serve as support of 0D nanomaterials for improving photocatalytic performance. *Appl. Catal., B* **2019**, *240*, 153−173.

(37) Acharya, L.; Nayak, S.; Pattnaik, S. P.; Acharya, R.; Parida, K. Resurrection of boron nitride in pn type-II boron nitride/B-doped-g-C_3N_4 nanocomposite during solid-state Z-scheme charge transfer path for the degradation of tetracycline hydrochloride. *J. Colloid Interface Sci.* **2020**, *566*, 211−223.

(38) Li, C.; Wu, X.; Shan, J.; Liu, J.; Huang, X. Preparation, Characterization of Graphitic Carbon Nitride Photo-Catalytic Nanocomposites and Their Application in Wastewater Remediation: A Review. *Crystals* **2021**, *11* (7), 723.

(39) Li, H.; Zhao, J.; Geng, Y.; Li, Z.; Li, Y.; Wang, J. Construction of CoP/B doped g-C_3N_4 nanodots/g-C_3N_4 nanosheets ternary catalysts for enhanced photocatalytic hydrogen production performance. *Appl. Surf. Sci.* **2019**, *496*, 143738.

(40) Qiu, Z.; Huang, N.; Ge, X.; Xuan, J.; Wang, P. Preparation of N-doped nano-hollow capsule carbon nanocage as ORR catalyst in alkaline solution by PVP modified F127. *Int. J. Hydrogen Energy* **2020**, *45* (15), 8667−8675.

(41) Mukherjee, M.; Samanta, M.; Ghorai, U. K.; Murmu, S.; Das, G. P.; Chattopadhyay, K. K. One pot solvothermal synthesis of ZnPc nanotube and its composite with RGO: A high performance ORR catalyst in alkaline medium. *Appl. Surf. Sci.* **2018**, *449*, 144−151.

(42) Ferrara, M.; Bevilacqua, M.; Melchionna, M.; Criado, A.; Crosera, M.; Tavagnacco, C.; Vizza, F.; Fornasiero, P. Exploration of cobalt@ N-doped carbon nanocomposites toward hydrogen peroxide (H_2O_2) electrosynthesis: A two level investigation through the RRDE analysis and a polymer-based electrolyzer implementation. *Electrochim. Acta* **2020**, *364*, 137287.

(43) Jia, Z.; Yin, G.; Zhang, J. Rotating ring-disk electrode method. In *Rotating electrode methods and oxygen reduction electrocatalysts*; Elsevier: Amsterdam, 2014; pp 199−229.

(44) Biddinger, E. J.; Knapke, D. S.; von Deak, D.; Ozkan, U. S. Effect of sulfur as a growth promoter for CN_x nanostructures as PEM and DMFC ORR catalysts. *Appl. Catal., B* **2010**, *96* (1−2), 72−82.

(45) Hossen, M. M.; Artyushkova, K.; Atanassov, P.; Serov, A. Synthesis and characterization of high performing Fe-NC catalyst for oxygen reduction reaction (ORR) in Alkaline Exchange Membrane Fuel Cells. *J. Power Sources* **2018**, *375*, 214−221.

(46) Kumar, Y.; Kumar, R.; Raizada, P.; Khan, A. A. P.; Van Le, Q.; Singh, P.; Nguyen, V. H. Novel Z-Scheme $ZnIn_2S_4$-based photocatalysts for solar-driven environmental and energy applications: Progress and Perspectives. *J. Mater. Sci. Technol.* **2021**, *87*, 234−257.

(47) Wang, D.; Pillai, S. C.; Ho, S. H.; Zeng, J.; Li, Y.; Dionysiou, D. D. Plasmonic-based nanomaterials for environmental remediation. *Appl. Catal., B* **2018**, *237*, 721−741.

(48) Zhang, H.; Wu, W.; Li, Y.; Wang, Y.; Zhang, C.; Zhang, W.; Wang, L.; Niu, L. Enhanced photocatalytic degradation of ciprofloxacin using novel C-dot@Nitrogen deficient g-C_3N_4: Synergistic effect of nitrogen defects and C-dots. *Appl. Surf. Sci.* **2019**, *465*, 450−458.

(49) Zhao, S.; Zhao, X. Insights into the role of singlet oxygen in the photocatalytic hydrogen peroxide production over polyoxometalates-derived metal oxides incorporated into graphitic carbon nitride framework. *Appl. Catal., B* **2019**, *250*, 408−418.

(50) Hu, J.; Chen, C.; Hu, T.; Li, J.; Lu, H.; Zheng, Y.; Yang, X.; Guo, C.; Li, C. M. Metal-free heterojunction of black phosphorus/oxygen-enriched porous g-C_3N_4 as an efficient photocatalyst for Fenton-like cascade water purification. *J. Mater. Chem. A* **2020**, *8* (37), 19484−19492.

(51) Lin, S.; Zhang, N.; Wang, F.; Lei, J.; Zhou, L.; Liu, Y.; Zhang, J. Carbon Vacancy Mediated Incorporation of Ti_3C_2 Quantum Dots in a 3D Inverse Opal g-C_3N_4 Schottky Junction Catalyst for Photocatalytic H_2O_2 Production. *ACS Sustainable Chem. Eng.* **2021**, *9* (1), 481−488.

(52) Dang, X.; Yang, R.; Wang, Z.; Wu, S.; Zhao, H. Efficient visible-light activation of molecular oxygen to produce hydrogen peroxide using P doped g-C_3N_4 hollow spheres. *J. Mater. Chem. A* **2020**, *8* (43), 22720−22727.

(53) Wei, B.; Wang, W.; Sun, J.; Mei, Q.; An, Z.; Cao, H.; Han, D.; Xie, J.; Zhan, J.; He, M. Insight into the effect of boron doping on electronic structure, photocatalytic and adsorption performance of g-C_3N_4 by first-principles study. *Appl. Surf. Sci.* **2020**, *511*, 145549.

(54) Bhagat, B.; Dashora, A. Understanding the synergistic effect of Co-loading and B-doping in g-C_3N_4 for enhanced photocatalytic activity for overall solar water splitting. *Carbon* **2021**, *178*, 666−677.